Three-dimensional structure of finite-amplitude ionization wave packets excited in He positive columns

K. Ohe, A. Naito, and T. Kimura
Department of Systems Engineering, Nagoya Institute of Technology, Showa-ku, Nagoya 466, Japan

N. Iwama
Department of Electronics and Informatics, Toyama Kenritsu Daiga-ku, Kosugi, Toyama 939-03, Japan

Spatiotemporal structures of large-amplitude ionization wave packets excited in a He positive column are reconstructed by the technique of computerized tomography (CT). The CT approach allows the use of sophisticated techniques to obtain radially resolved spectral images far superior to those from the more usual Abel inversion. Phenomena such as complicated ionization front interactions of the type modeled by Grabec [Phys. Fluids 17, 1834 (1974)] from the Pekarek equations are clearly seen.

I. INTRODUCTION

Ionization instability is one of the most common forms of instability in low-temperature plasmas such as the positive column of glow discharges. Here, the propagation phenomenon of the instability through the column is called the ionization wave, because the wave is excited by fluctuation in ionization. A distinct feature of the wave is that its phase velocity, which is directed toward the cathode, is opposite the group velocity in inert gases. After investigations of instability developed in the 1960s (then usually called striations) and were reviewed in some papers,[1-3] the feature continued to draw much attention and many important results were published.[4-6] A method[7] to excite a wave of stratification, i.e., a wave packet in a homogeneous positive column, greatly contributed to the establishment of the ionization wave theory. The ability to control the wave amplitude of the excited packet led to successful experiments concerning nonlinear behaviors such as a particlelike motion of the wave envelope,[8,9] which was theoretically predicted by wavelength prolongation due to the wave amplitude.[10]

On the other hand, particlelike motions of wave trains were simulated by numerically solving a set of hydrodynamic equations.[11] A large-amplitude wave which developed from a small Gaussian wave split into some large-amplitude impulse wave trains. Such a solitary wavelike behavior was predicted from the frequency shift to a higher one with an increase of the wave amplitude.[12] The behaviors of large-amplitude wave trains were first explained by Nedospasov and Petrov[13] on the basis of a phenomenological theory for ionization–diffusion relaxation. An early observation in a Ne positive column[14] revealed that wave trains with various amplitudes propagated with their own phase velocities, causing an overtaking between two adjacent waves with different phase velocities. A phase jump was observed before and after the overtaking. There still remain, however, some ambiguities in observation of such interaction processes.

The step ionization process related to the excitation mechanism of the ionization wave proposed by Pekarek and Krejci[15] brought to our attention the importance of detecting metastables. Donahue and Dieke[14] reported some spectroscopic observations associated with the ionization wave in a Hg–Ar positive column. The spectral line for the transition ^3p-^1s was spatially ahead of those for the mercury atoms in metastable states $^3p_0$ and $^3p_2$ in the wave propagation direction, following an increase in the positive space charge. Another observation of the wave excited in a Ne positive column indicated that the excitation phases were closely correlated with the excitation potential, enabling the inference of the first excitation of the spectral line with highest excitation potential.[16]

Although the profile of plasma density controlled by the radial density diffusion may have a strong effect on the ionization wave property, there have been only a few investigations[17] in the radial wave profile. A remote optical sensing technique may be more appropriate to detect the profile than the installation of probes because there is no disturbance to the plasma. The conventional detection method of the ionization wave using the optical radiation is a kind of remote sensing. Some techniques, for example, Abel's inversion and computerized tomography (CT), may be useful to detect the radial structure of the plasma column. Application[18] of Abel's inversion has been used to detect the radial density profile of the cylindrical plasma column. In detection of the wave phenomena, the CT technique is much better than Abel's inversion, because the former has an advantage in spatial resolution. After a pioneering application[19] of the CT technique to radiation from the plasma column to detect spatial structures of charged particle density, many improvements[20] led us to obtain useful information for the spatial structure of the varying emission in our positive columns. Recently, there was a successful attempt to reconstruct the radial structure of the light from an ionization wave excited in a He positive column.[21]

In the present paper we describe the three-dimensional structures of ionization wave packets excited in a He positive column reconstructed by our CT technique. The reconstruction system used here is the same as that previously described[21] except for a few modifications. Good imaging is obtained from nonspectroscopically and spectroscopically

resolved optical radiation using Phillips–Tikhonov (PT) regularization.[22] Nonlinear behavior of large-amplitude ionization waves is illustrated by reconstructed radial structures. The CT technique and the experimental system are described in Sec. II. Experimental results and discussion are presented in Secs. III and IV, respectively. In the final section we present a brief summary.

II. TECHNIQUE AND RECONSTRUCTION SYSTEM

The schematic diagram of the experiment is shown in Fig. 1(a). The positive column (diameter 5.5 cm, length 64 cm) is kept free from self-excited ionization waves by adjusting the pressure of helium gas and the direct discharge current. A wave packet, namely, a wave of stratification,[7] is excited by applying a 6 kHz sinusoidal burst voltage to a
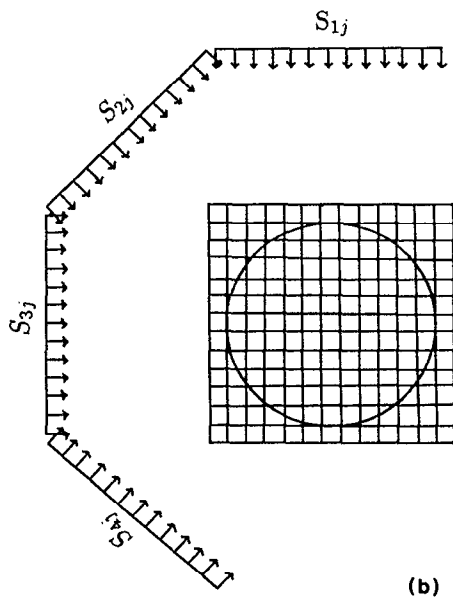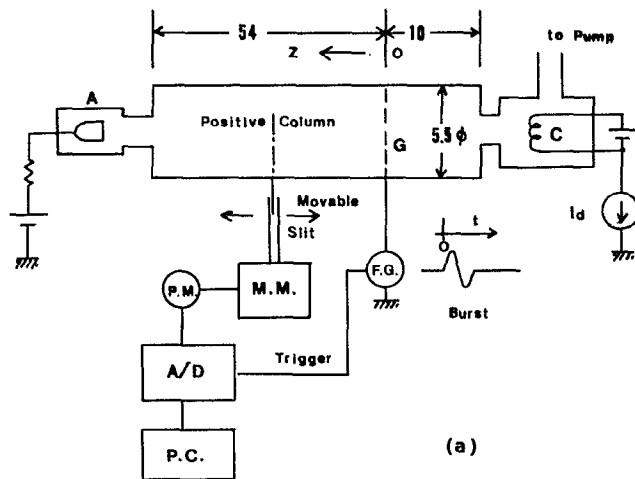

(a)

(b)

FIG. 1. Experimental setup. (a) Schematic diagram of experiment, F. G., function generator; M. M., monochromator; A/D, A/D converter; and P. C., personal computer. (b) Array of the projection data S_{ij}.

mesh grid installed 10 cm away from the cathode. The excitation is repeated with a frequency of 100 Hz at a discharge current 180 mA and a gas pressure 0.4 Torr. The optical radiation associated with the excited ionization wave packet is received with a slit-monochromator or a slit-photomultiplier that is movable along the tube axis and the radial direction. At each detection position the signal received is fed to an A/D converter and digitized with a sampling interval $\Delta t = 2.44$ μsec and amplitude resolution of 12 bits. The time-series signals registered on 128 successive wave packet excitations are averaged in the A/D converter to obtain a projection signal with a high signal-to-noise ratio. The details of the detection system are the same as the previous one[21] except for addition of the monochromator.

The time-series signals detected at seven positions equally spaced from the tube axis ($r = 0$) to the tube wall, ($r = 2.75$ cm) can be used as a set of projection data S_{ij} at 13 positions along the tube diameter because of the axial symmetry of the ionization wave.[21] The schematic figure of pixels to be reconstructed and the S_{ij} array, which is discussed later, are shown in Fig. 1(b). The spatial structure (radial structure) at a certain t is reconstructed from S_{ij} ($i = 4$, $j = 13$) by the Phillips–Tikhonov regularization,[22] which has countermeasures for errors in projection measurement. Thus $r - t$ spatiotemporal structures of the wave packet are reconstructed from S_{ij} time-series projection data. This procedure is followed repetitively at z positions, all of which are 0.5 cm from the grid to the anode, reconstructing $r - z$ spatial structures at a certain t.

III. EXPERIMENTAL RESULTS

Some typical $r - t$ structures of the wave packet at $z = 26$ cm are shown in Figs. 2(a)–2(c) with their respective contour maps, where I_t/I_{t0} is the ratio of the carrier wave amplitude in the packet to the steady-state measured by nonspectroscopically resolved radiation. The maximum wave crest and the minimum wave trough are divided by 20 equicontours. Small carrier waves are sinusoidal forms with a constant period as is inferred from the concentric circlelike contour in Fig. 2(a). On the other hand, the wave form becomes sawtoothlike with an increase of the wave amplitude, being accompanied by the period prolongation shown in Figs. 2(b) and 2(c). The wave amplitude causes the steepness in wave front and the increase in wave-front curvature in the radial direction as well. As previously described,[21] the wave front is intrinsically convex to the wave propagation direction.

The wave front of the wave component is obtained from surveying the results of reconstruction with respect to the temporal variations of image values at individual pixels.[21] From a series of radial wave profiles, the image in the central part of the discharge tube delays showing its temporal sinusoidal variation. Pursuing the variation in a pixel, a temporal wave pattern can be expressed in terms of the phase. Figure 3 shows the phase delay in the radial direction with respect to the reference set at the center $r = 0$ of the discharge tube for the small-amplitude wave as well as the large one. For the large-amplitude wave, the phase tends to lose its physical
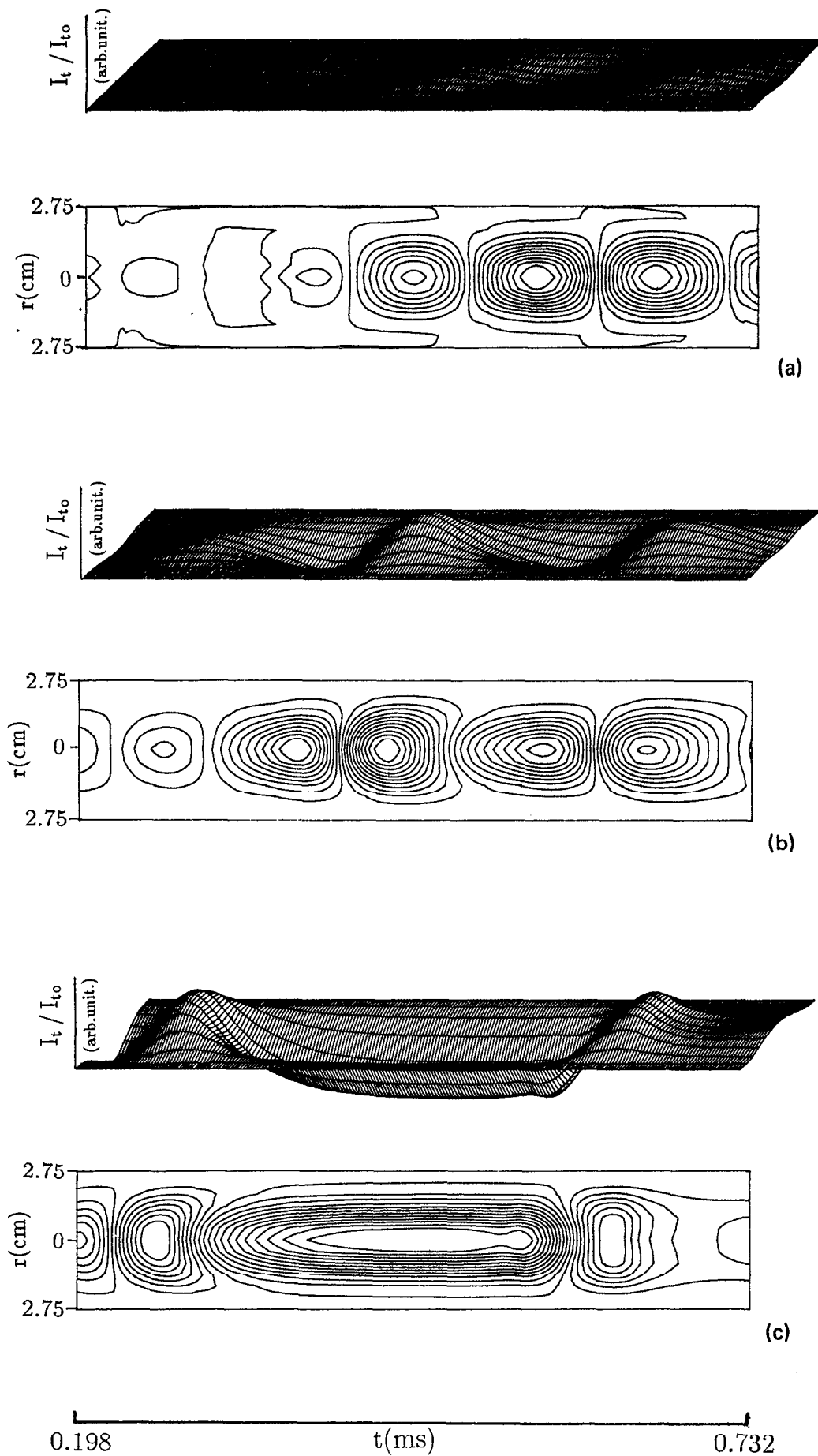
FIG. 2. $r - t$ structure of wave packet and its contour map for various I_{tm}/I_{t0}, where I_{tm}/I_{t0} is the ratio of the nonspectroscopically resolved maximum amplitude to the steady state. (a) $I_{tm}/I_{t0} = 0.09$; (b) $I_{tm}/I_{t0} = 0.38$; and (c) $I_{tm}/I_{t0} = 0.9$.
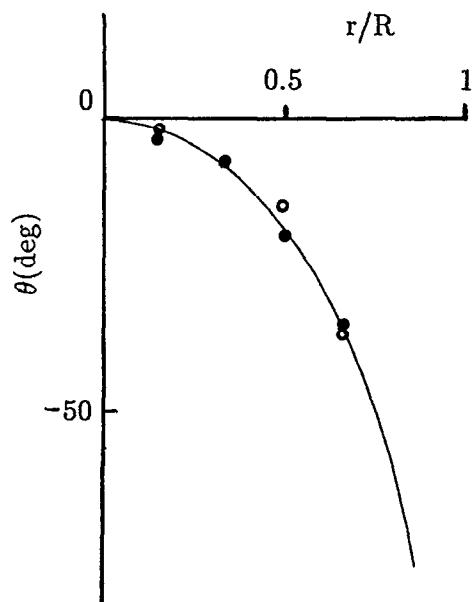
FIG. 3. Phase delays in the radial direction with respect to the reference at $r = 0$, where $\bullet$ is for $I_{tm}/I_{t0} = 0.24$, and $\bigcirc$ for 0.43. Solid curve is calculated by $\Phi = V_{x0} - V_r$.

FIG. 4. Radial profiles of I_{tm}/I_{t0}, where $\bullet$ is for $I_{tm}/I_{t0} = 0.42$, $\square$ for 0.40, $\triangle$ for 0.36, $\blacksquare$ for 0.22, and $\bigcirc$ for 0.15.

meaning because of the large deviation from the sinusoidal form. For comparison, the phase is evaluated for the fundamental wave component. The results show that the wavefront curvature for the large-amplitude wave is similar to that for the small one. The period prolongation between successive carrier waves due to the increase of wave amplitude seems to cause little apparent change in wave-front curvature, because the prolongation tends to conceal the increase, despite its size.

Radial profiles of I_{tm}/I_{t0} for various wave amplitudes are shown in Fig. 4, where each profile is normalized by respective I_{tm}/I_{t0} at $r = 0$, and the suffix m expresses the maximum value. The component I_{tm} for the small amplitude decreases in the radial direction more sharply than I_{t0}, whose radial profile is approximated by the zeroth-order Bessel function, while that for the large amplitude decreases more slowly, accompanied by an even smaller increase in the large-amplitude limit. The lens effect due to the cylindrical geometry of the discharge tube does not enable us to detect the profile near the tube wall with appropriate accuracy.

Space-series $r - t$ structures of the wave packet with large amplitude are shown in Fig. 5. The carrier waves become steep in the wave front with the propagation, sometimes causing a bifurcation of a wave, which occurs at a large-amplitude wave crest, the small peak being left behind while the large one gradually builds up toward the cathode. Alternative time-series $r - z$ structures of the carrier waves are shown in Fig. 6. The steepness in the wave front grows toward the cathode forming a sawtoothlike wave.

An ensemble of spatially resolved wave patterns detected at $r = 0$ is shown in Fig. 7. The slopes in the $z - t$ diagram of the wave crests increase with wave amplitude, corresponding to the increase in phase velocity V_p there. The $z - t$
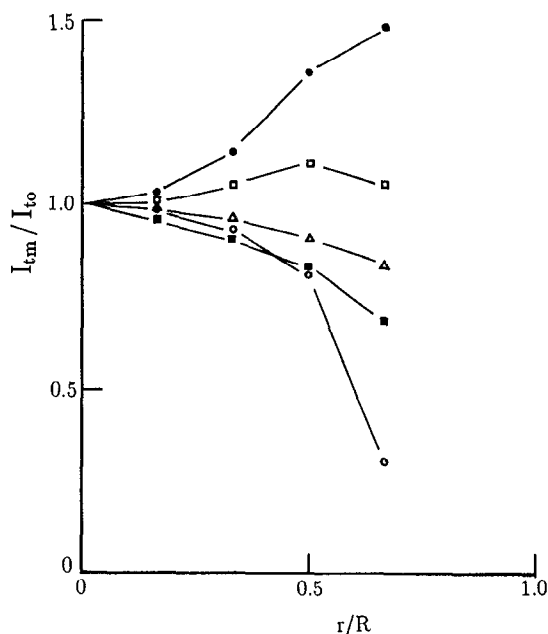
traces jump where a wave bifurcates. The dependence of V_p on wave amplitude is estimated from the slope of $z - t$ traces for various amplitude wave packets that are excited by various amplitude sinusoidal burst voltage, as is shown in Fig. 8. For extremely large-amplitude waves, the phase velocity V_p is approximately evaluated from a straight $z - t$ slope for a short interval without bifurcation. The larger the carrier wave amplitude is, the more rapidly the waves propagate in contrast to the small-amplitude waves with a constant V_p.

Some typical $r - t$ wave structures for the spectral lines and their contour maps are shown in Fig. 9, where I_s/I_{s0} is the ratio of the spectroscopically resolved wave component to the steady state. The reconstructed structures for a small-amplitude wave are similar to those shown in Fig. 2 except for some time delays among respective structures, whereas the structures for a wave of large amplitude are somewhat different. The 501.6 nm spectral line waveform, which is steeper in wave front than the 587.6 nm one, is evolved from the first rising 501.6 nm line. No clear difference can be detected between the wave-front curvatures of I_t and I_s. From waveforms for the seven spectral lines detected at $r = 0$, the spectral line of 501.6 nm rises with the minimum time delay at the wave front in contrast to the 587.6 nm line, which rises with the maximum delay, as shown in Figs. 10(a) and 10(b). There is some ambiguity in the wave amplitude detected due to the lack of sensitivity correction of the photomultiplier. Each spectral line decays with its own time constant in the wave tail without amplitude dependence. Dependence of I_{sm}/I_{t0} on I_t/I_{t0} is shown in Fig. 11, thus allowing us to deduce the large contribution of 388.9 nm line I_s/I_{s0} to I_t/I_{t0} from the direct proportion between them. A distinctive behavior of the 501.6 nm line (b) resulting from the first rise is observed from the relation. The linear relationships of I_t/I_{t0} for each line to I_{sm}/I_{s0} confirm that each
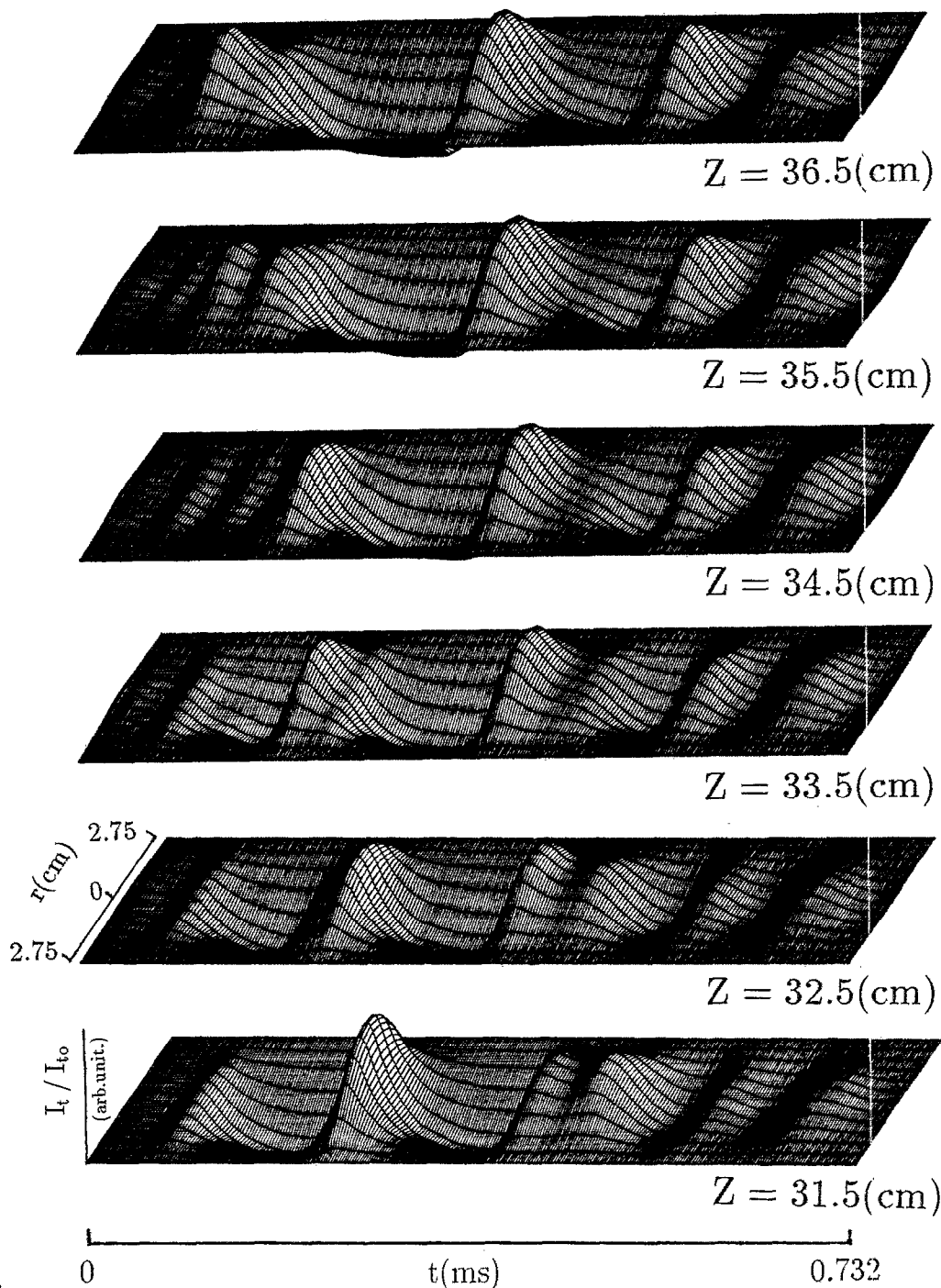
3305   Phys. Fluids B, Vol. 3, No. 12, December 1991

Ohe *et al.*   3305

FIG. 5. Space-series $r - t$ structures of a large-amplitude wave packet for $I_{tm}/I_{t0} = 0.9$.

Z = 36.5(cm)

Z = 35.5(cm)

Z = 34.5(cm)

Z = 33.5(cm)

Z = 32.5(cm)

Z = 31.5(cm)

spectral line rises and decays with its own time constant without wave amplitude dependence.

IV. DISCUSSION

Abel's inversion is a well-developed method to detect the internal structure of axially symmetrical plasmas such as a cylindrical positive column.[18] Then ionization waves through the column may be detected with a good resolution by the inversion. As is well known, CT technique requires no

axial symmetry assumption, which is a great advantage. Moreover, there have been many developments to improve the accuracy of image reconstruction. The spatially well-resolved structure can be reconstructed from finite acquired data by our CT technique, which has a countermeasure for measurement errors and a criterion to obtain the optimum image, as described in a previous paper in detail.[21]

The accuracy of reconstruction depends not only on the CT technique, but also the number of S_{ij}. The 13 projection data that correspond to $j = 13$ are sufficient to reconstruct
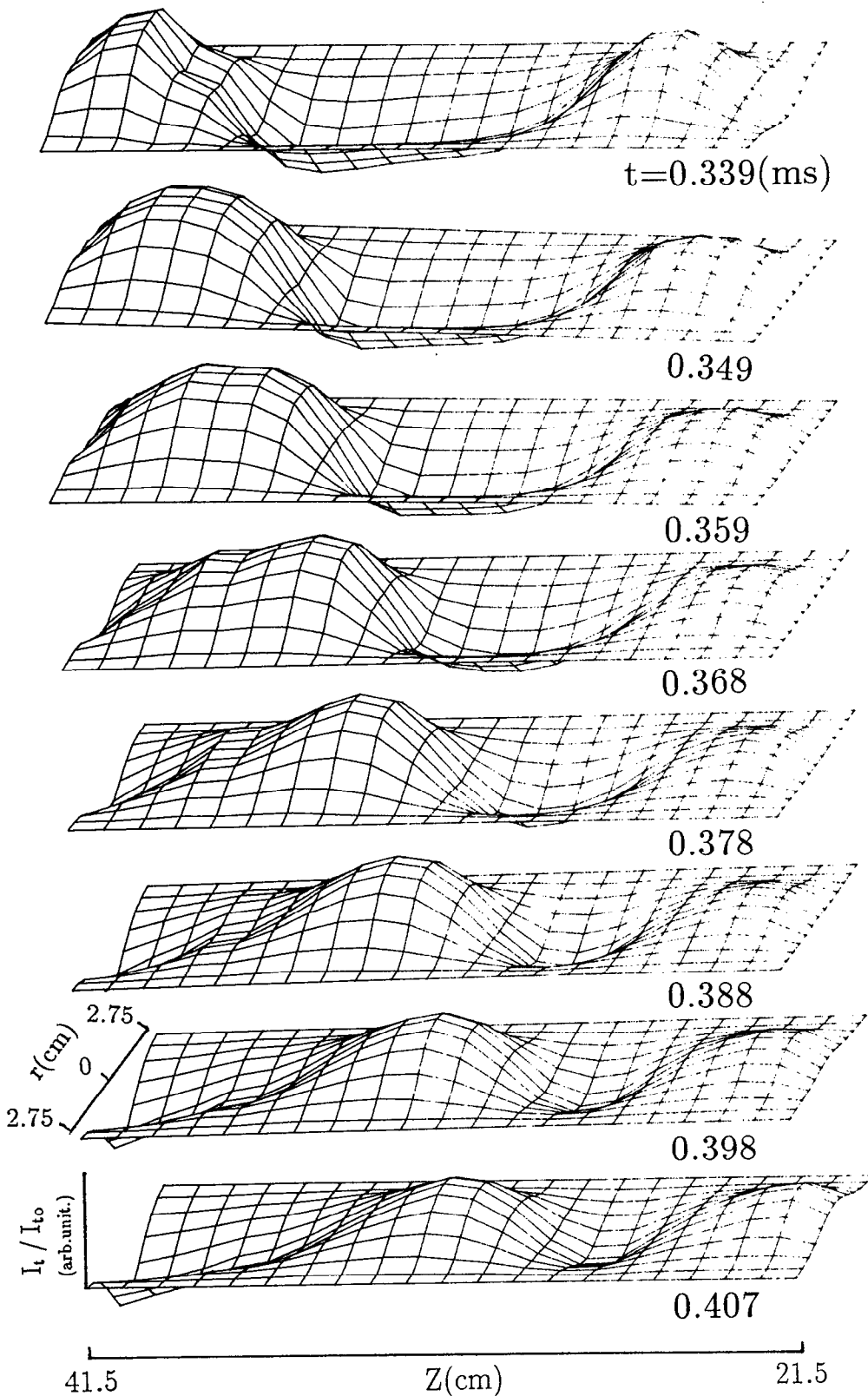
FIG. 6. Time-series $r - z$ structures of carrier waves for $I_{tm}/I_{t0} = 0.9$.

the packet[21] by the PT regularization method.[22] In order to obtain the optimal array of S_{ij}, three array sets are numerically simulated for a wavelike phantom: (1) S_{1j}-S_{2j} array with $\pi/2$ phase, (2) S_{1j}-S_{2j}-S_{3j}-S_{4j} array with $3\pi/4$ phase, and S_{1j}-S_{2j}-S_{3j}-S_{4j}-S_{5j}-S_{6j} array with $5\pi/6$ phase. From the

experiment, the second array is appropriate to reconstruct the accurate imaging.

Grabec's numerical simulation concerning the nonlinear behavior of each wave train[11] is an interesting development to analyze the nonlinear ionization waves. He showed
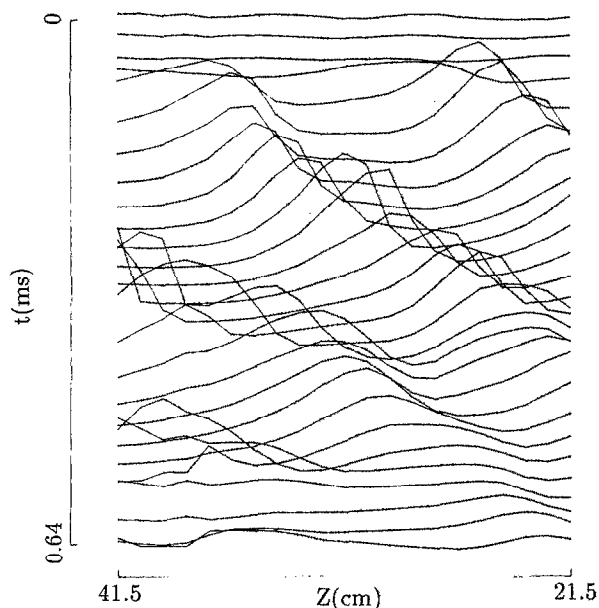
FIG. 7. Time-series spatially resolved wave patterns detected at $r = 0$ for $I_{tm}/I_{t0} = 0.9$. Thirty wave patterns detected at equal time intervals are shown in the abscissa with an arbitrary wave amplitude.

the nonlinear growth of a small Gaussian wave into some pulsive large-amplitude waves by solving Pekarek's equation. Dependence of the wave velocity on amplitude caused the nonlinear interaction between two adjacent wave trains, yielding a phase jump. The wave trains seemed to conserve their wave shapes before and after the interaction, eventually behaving like each peculiar soliton train. As shown in Fig. 2, both the steep wave front and the period prolongation in wave tail occur in the large-amplitude wave. To our knowledge, there has been no theoretical prediction of this phenomenon.
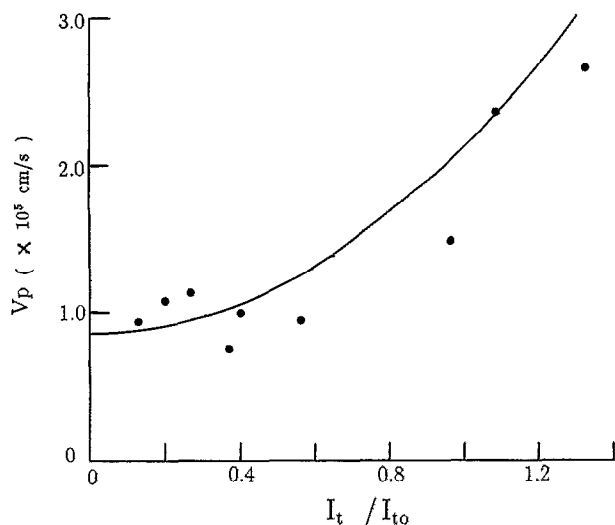
The nonlinear frequency shift to a higher one was theoretically deduced by taking account of the effect of ϵ^3 on ϵ, in which the reductive perturbation method was applied to a set of hydrodynamic equations.[12] The frequency ω_r for the optimal wavelength shifts into a higher one with the wave amplitude ϕ as follows:

$$\omega_r = \omega_o + \omega_n |\phi|^2, \tag{1}$$

where ω_o is the linear optimal frequency and ω_n the coefficient deduced from the nonlinear dispersion relation which is obtained from a set of hydrodynamic equations using a reductive perturbation method.[12] The phase velocity V_p for such a nonlinear wave can be calculated by disregarding the nonlinear wavelength shift,

$$V_p \doteq \omega_o/k_o + (\omega_n/k_o)|\phi|^2, \tag{2}$$

where k_o is the linear optimal wavelength. Equation (2), the numerical calculation of which is shown in Fig. 8, shows that the wave propagates with its velocity depending on the amplitude, eventually causing the steepness in wave front. The increase in radial curvature may result from the acceleration because the wave crest at $r = 0$ is much accelerated by its large amplitude.

Rather than any possible bifurcation, what seems most striking about the data of Fig. 7 is that it is qualitatively much like the numerical modeling of Grabec[11] (especially his Figs. 3 and 4 for ionization frequency and temperature, respectively). The qualitative agreement with Grabec's work is quite striking, even though Grabec set his system parameters to give very strong spikes that were even stronger than in the actual experiment. Particularly noteworthy are the sudden variations in peak velocity in both experiment and simulation, which do bear some resemblance to soliton-like overtaking-pulse interactions. However, a significant difference exists in the time behavior at a given location; in the experiment the pulse-to-pulse temporal correlation at a given location is much less pronounced than in Grabec's simulation.

The radial curvature convex toward the cathode shown in Fig. 3 was observed in He positive columns as well.[17,21] No account has been taken of the curvature in ionization wave theory so far. The electron temperature kT_e estimated by the Maxwell distribution for electrons and the axial electric field E_z can be assumed to be uniform over the whole column,[23] where k is the Boltzmann constant. The radial potential V_r is approximated except in the neighborhood of the tube wall as follows,[24]

$$V_r = - (kT_e/e)\ln(N_0/N_r), \tag{3}$$

where e is the electron charge, and N_0 and N_r are the electron densities at the tube axis and r, respectively. The equipotential Φ for a certain V_{z0} is estimated as $\Phi = V_{z0} - V_r$, where V_{z0} expresses the potential of the tube axis at z. We can assume that the ionization wave front propagates with the equipotential surface toward the cathode; the perturbation of Φ, which occurs at the surface, is directly related to the perturbation of E_z, and produces the electron density perturbation along the surface, consequently forming the ionization wave whose wave front is convex toward the cathode. Assuming that N_r decreases to the tube wall obeying the
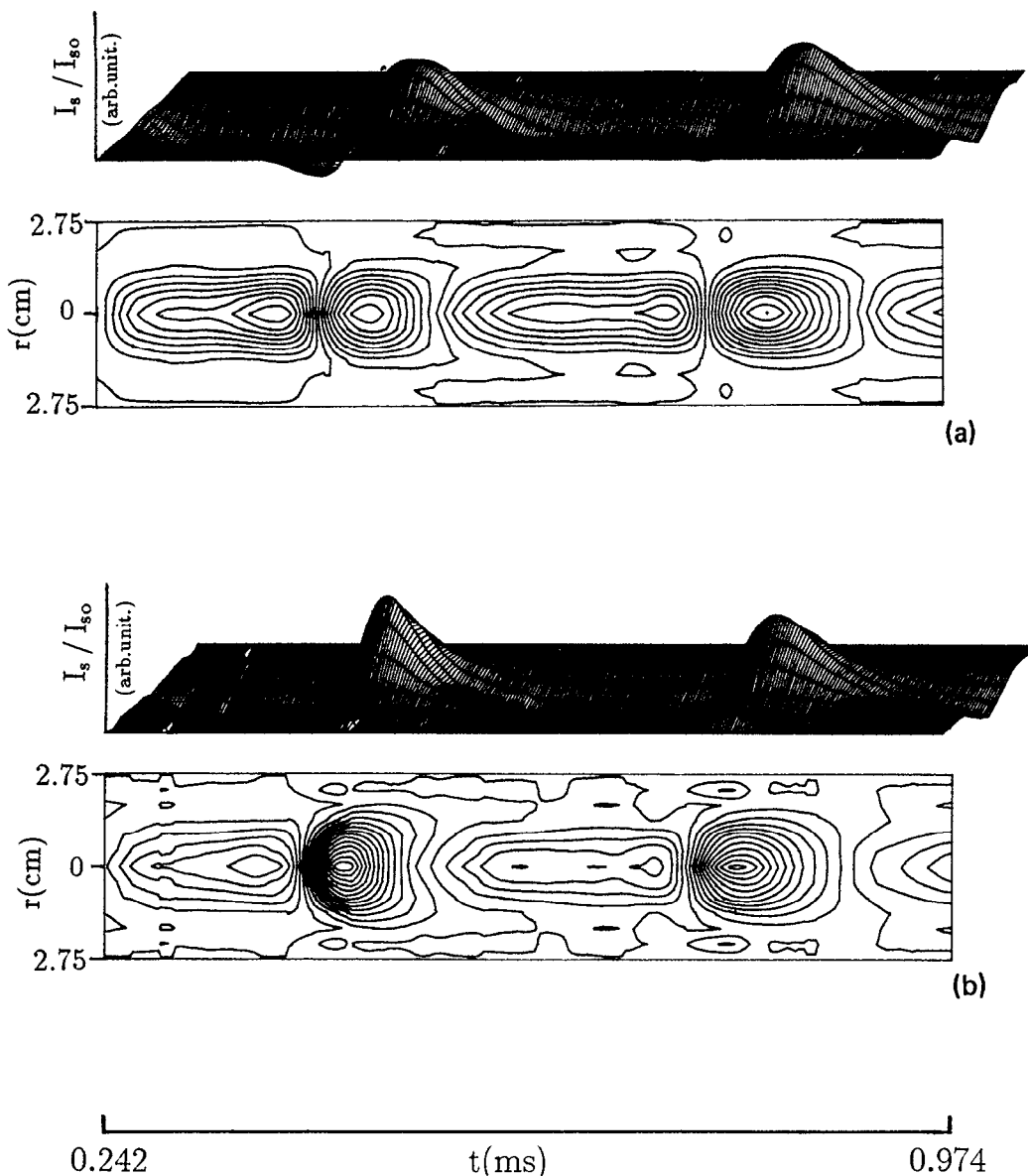

FIG. 8. Dependence of V_p on wave amplitude.

FIG. 9. $r - t$ structure and its contour maps for two spectral lines. (a) 587.6 nm and (b) 501.6 nm, where $I_{tm}/I_{to} = 0.43$.

zeroth-order Bessel function, the experimental values of kT_e = 3.26 eV, and E_z = 1.71 V/cm, Eq. (3) can be numerically calculated. Then the theoretical wave-front curvature can be evaluated by assuming that a sinusoidal wave with a radial curvature propagates with the equipotential surface, as shown in Fig. 3, where the wavelength λ experimentally obtained is 15 cm.

A report[16] indicated that the spectral line with the highest excitation potential was first excited at the ionization wave front in a Ne positive column. The results, which slightly differ from that of Ref. 16 as shown in Figs. 10(a) and 10(b), lead one to modify the above excitation mechanism. The 501.6 nm line, which rises first, stimulates the excitation of the 492.5 nm line in the singlet metastable state. In the triplet state, the 388.9 nm line, which rises first, stimulates the 471.3 nm line. The large radiation intensity of the 587.6 and 447.2 nm lines is due to the dominance in their populations when compared with the 471.3 nm case. The rise time of the 501.6 nm line, which is shorter than the 388.9 nm line, leads to the following mechanism by which the rise-time phase may depend on the slope of a plot of excitation cross section versus electron energy rather than the excitation potential, since the slope of a plot of singlet to triplet excitation cross section versus electron energy is larger than those that are singlet to singlet.[25] Further investigation of the spectral line excitation is necessary. The electric field is maximum around the wave crest causing the acceleration of electrons, whose energy is lost in the inelastic collision with neutral particles, and thus causing a large distortion of the electron energy distribution function.[26] Each spectral line in the wave tail decays a certain time constant as shown in Fig. 10. Such a decay can be inferred from the experimental results[27] that both metastables have similar diffusion coefficients.
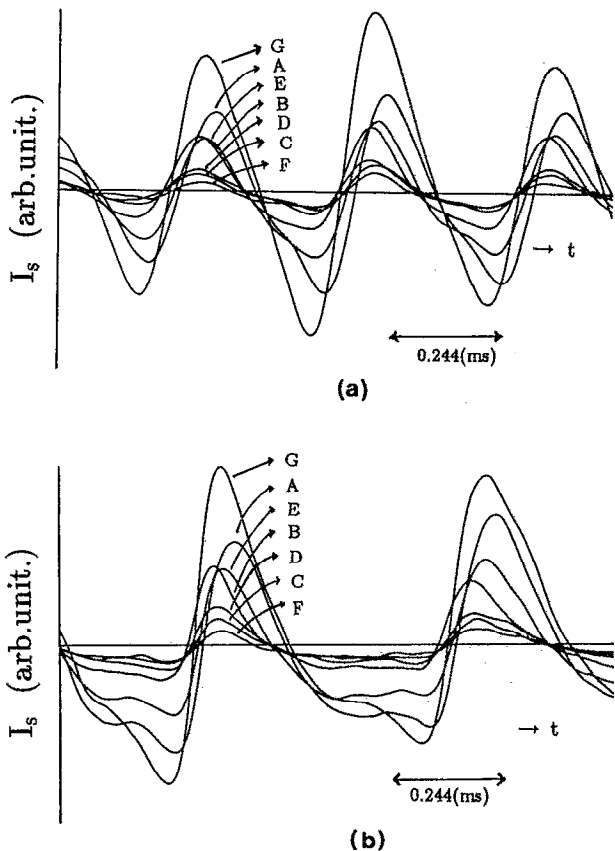
FIG. 10. Spectrally resolved temporal waveforms detected at $r = 0$ for (a) $I_{tm}/I_{t0} = 0.24$ and (b) 0.43, where A: is 587.6 nm, B: 501.6 nm, C: 492.5 nm, D: 471.3 nm, E: 447.2 nm, F: 402.6 nm, and G: 388.9 nm.
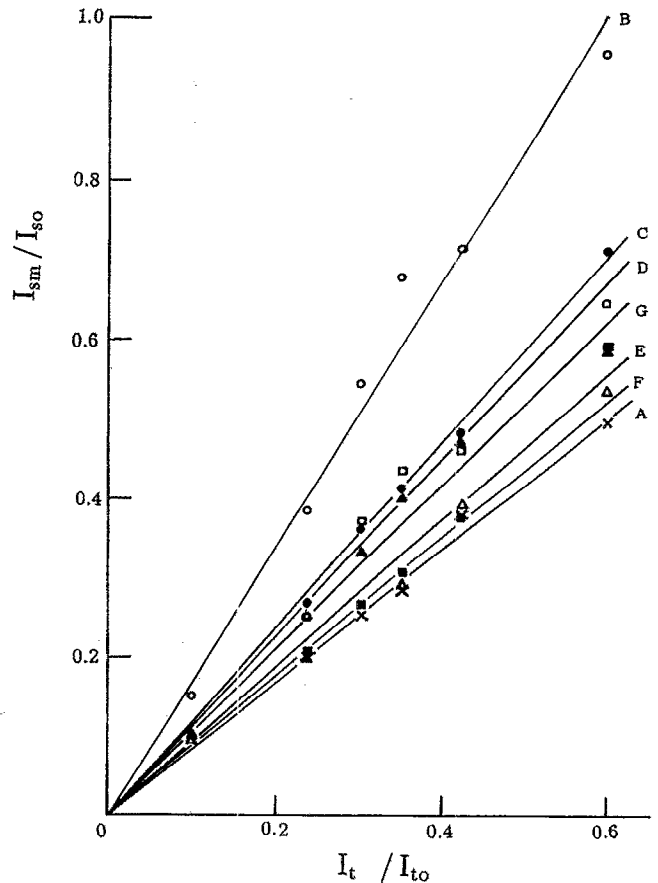

FIG. 11. Relationship between I_{sm}/I_{s0} and I_t/I_{t0}, where I_{sm}/I_{s0} is the ratio of the spectroscopically resolved maximum amplitude to the steady state.

V. SUMMARY

Spatiotemporal structures of finite-amplitude ionization wave packets excited in a wave-free He positive column are reconstructed from the optical radiation and its spectral lines by computerized tomography (CT). The CT technique by Phillips–Tikhonov regularization is useful to reconstruct good imaging of the wave packet. The results are summarized as follows.

(1) The increase in wave amplitudes causes steepness in wave front so as to form a sawtoothlike wave. The steepness may result from the acceleration of the phase velocity depending on the wave amplitude as predicted from the nonlinear dispersion relation.

(2) The wave-front curvature convex toward the cathode can be explained by the model in which the wave propagates with the equipotential surface caused by the radial plasma density gradient. The curvature increases with the wave amplitude.

(3) The $r - z$ structures of carrier waves show the formation of a sawtoothlike wave form toward the cathode, and a wave bifurcating into two as well.

(4) The spatiotemporal structures for each spectral line are similar to that for nonspectroscopically resolved radiation.

(5) Each spectral line rises up with its own time constant in the wave front, while the line decays with a certain time constant in the wave tail. The rise-time phase may depend on the slope of the excitation cross section.

ACKNOWLEDGMENTS

[1]A. V. Nedospasov, Sov. Phys. Usp. 11, 174 (1968).
[2]L. Pekarek, Sov. Phys. Usp. 11, 188 (1968).
[3]N. L. Oleson and A. W. Cooper, Adv. Electron. Electron Phys. 24, 155 (1968).
[4]A. Garscadden, Gas. Electron. 1, 65 (1978).
[5]L. Pekarek, Proceedings of the 10th International Conference on Ionized Gas Phenomena (Donald Parsons, Oxford, 1971), p. 365.
[6]P. S. Landa, N. A. Miskinova, and Y. V. Ponomarev, Sov. Phys. Usp. 23, 813 (1980).
[7]L. Pekarek, Czech. J. Phys. 8, 699 (1958).
[8]K. Ohe and M. Hashimoto, Phys. Fluids 27, 1863 (1984).
[9]K. Ohe and M. Hashimoto, J. Appl. Phys. 57, 822 (1985).
[10]M. S. Gorelik and L. D. Tsendin, Sov. Phys. Tech. Phys. 18, 478 (1973).

[11] I. Grabec, Phys. Fluids **17**, 1834 (1974).

[12] K. Ohe, T. Ogino, K. Asano, and S. Takeda, J. Phys. D **14**, 1009 (1981); K. Ohe, K. Asano, and S. Takeda, *ibid*. **14**, 1023 (1981).

[13] A. V. Nedospasov and V. G. Petrov, Sov. Phys. Tech. Phys. **19**, 31 (1974).

[14] T. Donahue and G. M. Dieke, Phys. Rev. **81**, 248 (1951).

[15] L. Pekarek and V. Krejci, Czech. J. Phys. B **12**, 296 (1962).

[16] N. L. Oleson and A. W. Cooper, Adv. Electron. Electron Phys. **24**, 178 (1968).

[17] K. Ohe and T. Kimura, J. Phys. D **22**, 266 (1989).

[18] See, for example, W. L. Baar, J. Opt. Soc. Am. **52**, 885 (1962).

[19] J. Schivell, IEEE Trans. Plasma Sci. **PS-8**, 226 (1980).

[20] See, for example, N. Iwama, H. Takami, S. Takamura, and T. Tsukishima, IEEE Trans. Plasma Sci. **PS-15**, 609 (1987).

[21] K. Ohe, A. Naito, and N. Iwama, Rev. Sci. Instrum. **61**, 2159 (1990).

[22] N. Iwama, H. Yoshida, H. Takimoto, Y. Shen, S. Takamura, and T. Tsukishima, Appl. Phys. Lett. **54**, 502 (1989).

[23] D. B. Ilic, J. Appl. Phys. **44**, 3993 (1973).

[24] A. von Engel, *Ionized Gases*, 2nd ed. (Clarendon, Oxford, 1965).

[25] M. Hayashi (private communication).

[26] K. Ohe and T. Kimura, Jpn. J. Appl. Phys. **28**, 1997 (1989).

[27] A. V. Phelps, Phys. Rev. **99**, 1307 (1955).